Geological mapping of the Menez Gwen segment at 37°50’N on the Mid-Atlantic Ridge: implications for accretion mechanisms and associated hydrothermal activity at slow-spreading mid-ocean ridges

M. Klischies[1*], S. Petersen[1], & C.W. Devey[1]

[1]GEOMAR – Helmholtz Center for Ocean Research Kiel, Wischhofstr. 1-3, 24148 Kiel, Germany

*Corresponding author: mklischies@geomar.de; Tel.: +49431-600-1430

Abstract

Slow-spreading mid-ocean ridges have the potential to form large seafloor massive sulphide (SMS) deposits. Current exploration for SMS deposits commonly targets associated active hydrothermal venting on the ridge axis, which makes the discovery of inactive vent sites and SMS deposits in the off-axis regions unlikely. Geological maps of the seafloor, which help understand the timing and location of SMS formation, usually focus on individual hydrothermal vent sites and their immediate surroundings, and are often too small to aid in SMS exploration. This study uses ship-based multibeam echosounder (MBES) data and a systematic classification scheme to produce a segment-scale geological map. When combined with spreading rate, this allows us to not only reconstruct the segment’s spreading history, but also reveals important processes that localize hydrothermal venting. Geological mapping around two known hydrothermal vent sites on the Menez Gwen segment at 37°50’N on the slow-spreading Mid-Atlantic Ridge showed that hydrothermal venting accompanies the tectonic break-up of a large, cooling magmatic body. Venting is focussed by faulting and resulting permeability changes. The large magmatic body is associated with an axial volcano that formed as a last stage of a period with intense magmatic accretion. Such magmatic accretion periods occur every 300 to 500 ka at the Menez Gwen segment, with increasing intensity over the past 3.5 Ma years. The most recent, most intense magmatic period appears to be a regional phenomenon, also affecting the neighbouring Lucky Strike and Rifted Hills segments. Understanding the accretional setting

and the spatial and temporal constraints of hydrothermal venting enables us to develop criteria in MBES data to aid exploration for inactive SMS deposits.

Keywords

Slow-spreading mid-ocean ridge, hydrothermal venting, multibeam echosounding, geological mapping.

1. Introduction

Slow-spreading ridges (20 mm/a to 55 mm/a, Baker, 2017) dominate the global mid-ocean ridge system and have the largest sulphide potential of known hydrothermal vent systems (Hannington et al., 2005, Beaulieu et al., 2013, German et al. 2016). This is likely due to their heavily tectonized upper crust that provides sufficient permeability to promote stable, long-term hydrothermal circulation (Parson et al., 2000, Canales et al., 2007, McCaig et al., 2010). Nevertheless, hydrothermal venting on slow-spreading ridges is limited to specific locations (Baker and German, 2004), although the processes that determine the timing and location of vent fields remain unclear. Only a few studies consider the regional, segment-scale context of hydrothermal systems (e,g., Escartín et al., 2014, Escartín et al., 2015, Escartín et al., 2017, Eason et al., 2016, Anderson et al., 2017).

This study focuses on the Menez Gwen segment (Fig. 1), which hosts two on-axis, basalt-hosted hydrothermal systems with venting temperatures at or close to the boiling curve of seawater: the Menez Gwen vent field at around 800 m water depth, and the Bubbylon vent field at 1000 m water depth (Fouquet et al., 1994, Fouquet et al., 1995, Borowski et al., 2010, Dubilier et al., 2012, Marcon et al., 2013). The Menez Gwen segment is part of the slow-spreading Mid-Atlantic Ridge (MAR) and shows recent, substantial hotspot-influenced volcanic activity (Fouquet et al., 1994, Ondreas et al., 1997, Thibaud et al., 1998, Dosso et al., 1999, Yang et al., 2006). German and Parson (1998), and Gràcia et al. (2000) proposed that hydrothermal activity may be focused within non-transform discontinuities (NTDs) in this part of the MAR; but, up to present, the NTDs around Menez Gwen lack indications of hydrothermal activity.

Geological maps of the seafloor have been used to aid resource and hazard assessment, but also habitat mapping and other disciplines. Nevertheless, only a global-scale geomorphologic classification of deep sea bathymetry exists (Harris et al., 2014) and systematic geological characterization of mid-ocean ridges is lacking. This study uses a classification scheme to systematically translate ship-based multibeam bathymetry information into a segment-scale geological map.

The resulting first geological map of the Menez Gwen segment is used to resolve spatial and temporal variations of crustal accretion mechanisms at this slow-spreading mid-ocean ridge. This study analyses where and when hydrothermal circulation is established with the aim of improving our understanding of the setting and conditions determining the timing and location of hydrothermal venting.

2. Geological Setting

The Menez Gwen segment is located at 37.5°N on the MAR, south of the Azores Hotspot (Fig. 1). In this area, the MAR spreads symmetrically at a full-spreading rate of ~19.6 ± 0.2 mm/a (Argus et al., 2011), although magnetic anomalies indicate a slightly higher spreading rate of ~24.0 mm/a between anomaly 2A and 3 (2.45 to 3.85 Ma ago; Luis et al., 1994).

Together with the Lucky Strike segment to the south and the Rifted Hills segment to the north, the Menez Gwen segment belongs to the Azores Volcanic plateau (German et al., 1995, Cannat et al., 1999). Right-stepping non-transform discontinuities (NTDs) separate these three segments, and other ridge segments south of the Azores. The Princess Alice Offset bounds the Menez Gwen segment to the north and the Pico Offset separates Menez Gwen from the Lucky Strike segment. These zones accommodate strike-slip movements, ridge-oblique faulting and rifting. They typically show heavily-faulted seafloor, substantial talus and sediment cover, nodal basins, and are associated with thin, cold crust (Fig. 2a; Detrick et al., 1995, Gracia et al., 2000, Parson et al., 2000).

All three segments are characterized by relatively shallow water depths, a pronounced volcanic axial high, and thickened crust in the segment center due to enhanced, hotspot-influenced magmatic accretion (Detrick et al., 1995, Ondreas et al., 1997). Both the Menez Gwen and the Lucky Strike segment host hydrothermal systems (Fouquet et al., 1995, Escartín et al., 2015). The segment-centered Menez Gwen axial volcano (Fig. 2a) is about 17 km wide, 700 m high, and reaches water depths of less than 700 m (Fig. 2). The topography and a strong positive gravity anomaly suggest thick crust at the segment center underneath the axial volcano (Detrick et al., 1995). An axial graben rifts the entire volcano structure, hosting a drained lava lake and young volcanism (Fig. 2a). The graben structure is about 2 km wide and up to 400 m deeper than the surrounding volcano flanks. The graben walls expose sheet flows overlain by volcanic ejecta (Fouquet et al., 1994). In general, the magmas from the Menez Gwen segment are enriched in mantle-incompatible elements (E-MORB, Dosso et a., 1999, Marques et al., 2009). Hydrothermal venting (up to 280°C) at the Menez Gwen segment was discovered in 1994 at about 850 m water depth on the southern flank of a small, young volcano within the axial graben, also named Menez Gwen (*DIVA-1* cruise, Fouquet et al., 1994) and referred to hereafter as 'Menez Gwen cone'. These vent sites lie within the protected area of the Azores Marine Park. Additional venting in the Menez Gwen vent field occurs a few tens of meters upslope (outside the marine protected area), at 830 m water depth near the summit of the Menez Gwen cone, and includes a series of small vent sites that cover up to 200 m^2 of seafloor (Marcon et al., 2013). Here, clear to milky fluids are venting from small anhydrite chimney structures (up to 50 cm tall) at temperatures of up to 300°C, close to the boiling curve of seawater at this depth (Dubilier et al., 2012). Associated hydrothermal precipitates and crusts are barite-rich and sulphide-poor (Lein et al., 2010, Dubilier et al., 2012). Geochemical analyses of fluids and precipitates suggest phase separation in the subsurface (Charlou et al., 2000, Bogdanov et al., 2005, Lein et al., 2010, Marcon et al., 2013) and a direct contribution of volatiles to the hydrothermal fluids from a degassing magma chamber underneath Menez Gwen (Marques et al., 2011). The high gas contents of the hydrothermal vent fluids enabled acoustic detection of the hydrothermal plume above the young volcano in multibeam water column data during a cruise of R/V “Meteor” in 2010 (Dubilier et al., 2012). Additional reflections in the water column data indicated several gas plumes along the eastern and western bounding faults of the axial graben. Subsequent ROV dives tied one of these anomalies to a previously unknown active hydrothermal vent site, named “Bubbylon”. This vent site is located at 1000 m water depth, about 5 km south of the Menez Gwen vent sites, and located on talus material covering an east-facing fault scarp in the southwestern part of the axial graben (Dubilier et al., 2012). Venting temperatures reach up to 295°C, which is below the boiling curve of seawater (Dubilier et al., 2012). The associated precipitates are mineralogically similar to those of the Menez Gwen hydrothermal field.

3. Methods

Geological mapping based on ship-based MBES bathymetry and acoustic backscatter intensity enables the reconstruction of volcano-tectonic processes at mid-ocean spreading centers on a regional scale (Anderson et al., 2016, Anderson et al., 2017, McClinton et al., 2013, Yeo et al., 2016). Previous mapping exercises at Menez Gwen were based on lower resolution, lower coverage bathymetry than the data used for this study, but were complemented by dive observations providing ground truth data (Parson et al., 2000, Gracia et al., 1997). This study develops a systematic classification scheme for remotely sensed data and broadens and refines the findings and ground truth information of previous studies to a segment scale. This allows a reconstruction of a regional, segment scale picture of magmatic, tectonic, and hydrothermal processes at the slow-spreading Menez Gwen segment.

3.1 Data acquisition and processing

This study is based on a multibeam data set acquired during R/V *Meteor* cruise M82/3 in 2010 (Dubilier, 2013). The mapped area covers about 2900 km² of seafloor along nearly 100 km of the MAR, extending to crustal ages of up to approximately 3.5 Myrs (Fig. 1). Two shipmounted sonars were used: the *Kongsberg EM 122* (12 kHz) mapped seafloor below 1000 m water depth, while the *EM 710* (70 to 100 kHz) was used for mapping in shallower water around the central volcano. This resulted in two different digital elevation models (DEMs): a DEM with 30m spatial resolution covering the entire Menez Gwen segment up to 35km off-axis, and a second DEM with 10m spatial resolution covering the axial graben in the center of the Menez Gwen segment (Fig. 2). Data processing was conducted with the *FLEDERMAUS* software suite (QPS Canada Inc., Version 7) on shore.

Seafloor slope and rugosity were calculated from the 30m DEM. The slope map, calculated with the software "*Global Mapper"* (Blue Marble Geographics, Version 18) in a three by three cell range, indicates slopes ranging from 0° to 30° in greyscale colors (white to black). The slope maps shade the bathymetric maps, presented here (e.g., Fig. 2a).

A mosaic of multibeam acoustic backscatter data was produced using the FMGT module of *FLEDERMAUS*. The mosaic achieves a spatial resolution of 18 m with lighter grey-shades representing higher backscatter intensities (Fig. 2b). Backscatter data from slopes ≥30° is biased (due to the incidence angle) and is not used in our interpretations.

3.2 Systematic classification

DEM-based analysis of seafloor geomorphology is the foundation of the geological classification we developed. Previous mapping attempts based on TOBI side scan data (Gràcia et al., 2000), and lower resolution bathymetry data (Ondreas et al., 1997) complement the geomorphological analysis. Further, ground truth data from dive observations (manned submersible *Nautile*: Fouquet et al., 1994, Ondreas et al., 1997; ROV dives: Borowski et al, 2010, Dubilier et al., 2012, Marcon et al., 2013), and dredging (Marques et al., 2009) helped guide the interpretation in some places. The geological setting, known magmatic, tectonic, and sedimentary processes, and previous observations determined the geological naming scheme.

Backscatter intensities depend on the topography of the seafloor, but also on the physical properties of the reflecting substrate; therefore, backscatter information can enhance the geomorphological interpretation or lead to the formation of subclasses (see Fig. 3). High backscatter intensities suggest bare, young rock surfaces, while low intensities imply a soft (sediment) cover (Eason et al., 2016). Assuming temporally and spatially constant sedimentation rates and similar incidence angles, backscatter intensities can also provide relative ages.

Analysis and digitization were conducted manually in "*ArcGIS*" (Esri, Version 10.4). An overview of all mapped features, terrain types, and identification characteristics is given in Table 1 and is described in the following.

3.2.1 Elementary seafloor features

Analogous to terrestrial geomorphological analyses (e.g., Minár & Evans, 2008), the simplest and most distinct morphologies are classified in our mapping scheme as elementary features. The different types of elementary features recognized are shown in ***bold*** below:

Scarps, or overall linear steps in topography with distinct slope changes define ***faults***. Their trace follows the outcropping contact between hanging block and footwall. Asymmetries in cross sections determine dipping directions of faults. ***Lineaments*** trace distinct, linear slope changes without any definable dip. Round, dome- to cone-shaped constructions with steep flanks are classified as ***volcanic cones*** that are outlined by the slope change at the bottom of their flanks (following Grosse et al., 2012). In addition to their overall volcanic shape, ***flat-topped volcanoes*** have a wide, flat summit and a specific height to width ratio close to 1:10 (Clague et al., 2000). Volcanic ***craters*** are funnel-shaped depressions on or within the summit area of volcanic forms; the crater outline follows the slope change of the crater rim.

Backscatter intensities of fault scarps vary, depending on the slope angle. Volcanoes are generally associated with high backscatter intensities, although the wide summits of flat-topped volcanoes often show relatively low intensities.

3.2.2 Terrain types

Specific patterns of attributes, derived from the DEM (in this case slope and rugosity), characterize areas of similar and commonly found morphologies, and allow us to designate terrain types (see Fig. 3). Where applicable, terrain type classification is also supported by analysis of backscatter intensities (see Table 1). Elementary features often function as boundaries between different terrain types due to their distinct changes in attributes (Minár & Evans, 2008).

Wide areas of relatively flat seafloor with low rugosity and low, homogenous backscatter intensities characterize ***sedimented plains***. ***Sheet flow*** terrain is geomorphologically similar to the sedimented plains, but is spatially limited and shows high backscatter intensities. ***Hummocky flows and mounds*** combines terrain with an overall positive relief, indefinite depressions, and many small (cone-shaped) mounds on a smaller scale (Yeo et al., 2012, Clague et al., 2017). Rounded, interlinked forms in the rugosity pattern are characteristic for hummocky terrain. Slope is also very variable within this terrain type. Backscatter intensities of hummocky terrain appear patchy due to the rough relief, but are in general intermediate to high. The ***neo-volcanic zone*** contains hummocky terrain, lava flows and volcanoes, but all with very high backscatter intensities. ***Sedimented hummocky terrain*** designates geomorphologies similar to hummocky terrain, but with less variability in relief and a generally smoother appearance. Backscatter intensities are patchy on a small scale and, on average, lower than those of hummocky terrain. ***Off-axis highs*** indicate elevated provinces with morphologies similar to sedimented hummocky terrain. Large, and extensive faults disrupt this hummocky surface. Backscatter intensities of off-axis highs are patchy, and vary between high and low. ***Blocky terrain*** is the term given to rough, heavily disrupted terrain forming elongated highs and depressions of various sizes. Related backscatter intensities are low to very low, with patches of slightly higher intensities coinciding with small elevations or fault scarps. Structureless, rough forms in small, elongated to fan-shaped patches of positive relief that align along fault scarps or slopes define ***talus***. Recorded backscatter intensities of talus fans show no distinct pattern or range.

3.3 Inferred units

Inferred units summarize and interpret the mapped elementary features and terrain units in a first step to capture the most important geological features of a ridge segment. Dipping directions of faults determine the ***ridge axis***, as the majority of fault scarps face inwards in a slow-spreading ridge environment (McAllister & Cann, 1996, Buck et al., 2005). High backscatter intensities from potentially young, volcanic rock surfaces without sediment cover (neo-volcanic zone) support the determination of the ridge axis. Identifying the ridge axis is crucial for further age calculations (see below).

The ***inner rift wall*** and ***outer rift wall*** comprise fault zones which bound the rift valleys and localize tectonic strain over time (McAllister & Cann, 1996). They are typical for slow-spreading mid-ocean ridges. Following the definition of Searle et al. (2010), an ***axial volcanic ridge*** (AVR) comprises hummocky and volcanic units located on the ridge axis, with an overall segment scale extent, a width of a few kilometers, and height of a few hundred meters.

An ***axial volcano cone*** unit is restricted to the segment center and defined by a round, cone shape (neglecting the axial graben) and a very smooth, slightly inclined surface. The ***axial volcano base*** unit comprises elevated, slightly inclined terrain with a texture of lobes pointing away from the volcano summit, and only minor ridge-parallel faulting.

3.4 Spreading age calculations

The inferred ages of mapped units presented here are based on their orthogonal distance to the ridge axis combined with a half-spreading rate of, on average, 10.0 mm/yr (DeMets et al., 2010). We call this their ‘spreading age’. Magnetic anomalies record symmetric spreading activity that has been assumed to be constant in speed for the majority of the investigated time interval (Luis et al., 1994, Cannat et al., 1999; Argus et al., 2011). For segment-scale features, eleven across-axis profiles with an average spacing of 5 km were analysed to determine spreading ages.

The neo-volcanic zone defines the area of current magmatic accretion, and due to its width and hour-glass shape introduces an error of +/- 100 kyr to the calculated spreading ages at the segment center and an error of +/- 150 kyr at the segment ends (average of +/- 120 ka). A further source of error in the spreading ages comes from the fact that measured distances to the ridge axis consider neither stretching caused by extension (i.a., normal faulting), nor additional offsets due to the overall dome-like shape of mid-ocean ridges.

Age considerations focus on ridge-axis-parallel features, as inside corner structures are potentially affected by NTD dynamics. The distance of faults to the ridge axis can be precisely measured. Spreading ages for faults equal the ages of the deformed crust, and hence, represent the maximum possible age of tectonic deformation. Periods of volcanic activity consider the ages of covered, affected crust and hence, give the maximum possible time span for a volcanic period. If volcanic edifices are ruptured by faults, the initiation of tectonic deformation marks the time of vanishing volcanic activity.

4. Results

The geological map of the Menez Gwen segment (Fig. 4) is the first geological map of a slow-spreading mid-ocean ridge segment produced from ship-based MBES data using a systematic mapping scheme for manual delineation. The map contains two linear feature classes, 17 polygonal units, and four interpretative units (ridge axis, inner and outer rift wall, axial volcanic ridge) summarizing prominent features, as describe below.

4.1 Tectonics

Over one thousand faults and lineaments were digitized (Fig. 4). Water depths of less than 1900m and a ridge-parallel fault pattern dominate a 30 km long section of the MAR and define the ‘Menez Gwen segment’ (average fault strike of N020, Fig. 4a).

In the north and in the south, the fault strike rotates clockwise towards the bounding NTDs into a ridge-oblique, northeast-southwest trend, while the seafloor simultaneously and significantly deepens. These areas are summarized in the term ‘NTD provinces’, used in the following,

Two pairs of ridge-parallel, opposing fault zones form a graben sequence with an inner and an outer rift valley (Fig. 4a). The fault zones, summarized as rift valley walls, accommodate a throw of 100-400 m each. The outer rift valley is about 20 km wide. The inner rift valley has a width of 2-5 km and ruptures both the on-axis hummocky terrain and the Menez Gwen axial volcano (Figs. 4 and 5). The central part of the inner rift valley corresponds to the axial graben hosting the two known hydrothermal systems of the segment.

The axial graben shows the highest fault density of the segment, which is calculated as the kernel density of digitized faults within a search radius of 2000 m for a raster cell size of 30m in ArcGIS. In the axial graben, faults are short and mainly associated with talus fans or the axial graben walls (Fig. 5). In between the two hydrothermal systems, only a few faults could be identified from MBES data (see Fig. 5b). In the off-axis areas, sedimentation may obscure small-throw faults even beyond the sedimented plains, thereby limiting the delineation of faults and partially decreasing the calculated fault density.

At the inside corners of both NTDs, off-axis high terrain shows very high fault densities (Fig. 4a). Cross-cutting, NTD-parallel faults and graben structures contribute to the high fault density in this area.

4.2 Magmatism and hydrothermal venting

As on land, submarine extrusive volcanism forms various types of geomorphologies. Besides characteristic cone-shaped volcanoes, also flat-topped volcanoes, hummocky and sedimented hummocky terrain, and lava flows could be mapped (Fig. 4b). In total, 144 digitized volcanoes were identified. Of these, 32 edifices (22 %) are flat-topped volcanoes. Another 14 volcanoes (10 %) show cratered summits. In addition to the rifted large axial volcano, 6 rifted halves of former volcanic cones are identified (Fig. 4b and 5b).

On average, flat-topped volcanos are larger in diameter than cone-shaped volcanoes. Smaller volcanic structures (<1 km in diameter) are usually confined to the neo-volcanic zone (Fig. 4b). Volcanic morphologies were detected throughout the entire Menez Gwen segment with the exception of the NTD regions. A single, cratered, cone-shaped volcano, about 2.5 km wide, occurs within the Pico Offset surrounded by lava flows (Fig. 4b).

4.2.1. Menez Gwen axial volcano and hydrothermal venting

The most prominent volcanic feature of the segment is the axial Menez Gwen volcano itself (Fig. 5). It occupies the center of the segment and is rifted by the inner rift valley and axial graben. Similar features are not observed in the mapped off-axis areas.

The transition between volcanic morphology related to the Menez Gwen axial volcano and the adjacent or underlying AVR is gradual, especially within the first 300 to 400 m rising above the surrounding sedimented plain (axial volcano base, Fig. 4 and 5). In contrast, the top-most 500 m of the axial volcano flanks protrude from the (sedimented) hummocky terrain of the AVR and show a continuous, smooth morphology and low rugosity with a relatively constant slope, coinciding with moderate backscatter intensities (Fig. 4 and 5).

At the center of the axial volcano and graben, a patch of relatively flat seafloor shows unusually high backscatter intensities. As the location and dimensions of this patch coincide with a ca. 50 m deep depression in the bathymetry and the visual observation of a drained lava lake, this patch of flat seafloor is classified as a 'drained lava lake' (Fig. 5; Fouquet et al., 1995, Ondreas et al., 1997).

North of the drained lava lake, several young volcanoes occupy the neo-volcanic zone. The largest edifice is the Menez Gwen cone, which is 200 m tall, about 1200 m wide, and is filling the entire across-axis width of the neo-volcanic zone (Fig. 5 and 6). The Menez Gwen vent field is located at 800 m water depth near the faulted summit of the volcano.

South of the drained lava lake, small talus fans narrow the neo-volcanic zone to about 1 km in across-axis width. There, the Bubbylon vent field is located in 1000 m water depth on the terraced western graben wall fault. With the exception of a single small volcanic edifice, the surrounding area lacks prominent volcanic features (Fig. 4b and 6).

4.2.2. Past and present axial volcanic ridges of the neo-volcanic zone

Along the spreading center, hummocky terrain is the dominant terrain type. The along-axis relief of the neo-volcanic zone is dome-shaped and ranges from over 2200 m water depth at the NTDs to less than 1000 m water depth in the axial graben. The neo-volcanic zone coincides with the highest backscatter intensities (Fig. 2b).

On-axis, hummocky terrain and sedimented hummocky terrain form a 50 km long, up to 5.5 km wide and 100–400 m high ridge, which merges into the axial volcanic ridge (AVR, Fig. 2 and 4b) following the definition by Searle et al. (2010). The AVR extends beyond the 30 km long Menez Gwen segment, protruding into the deeper, ridge-obliquely faulted NTD provinces (about 10 km into each NTD; Fig. 4). The AVR and the inner rift valley bend and align with the prevailing ridge-oblique, northeast-southwest trend of the NTD-related structures. Most of the terrain mapped as lava flows occurs near the inside-corner margins of the bending AVR tips.

Off-axis highs extend along the entire segment length, and show an overall relief and terrain types comparable to the AVR (Fig. 4 and 6). Extensive faults rupture off-axis highs and form their inward facing boundaries.

At NTD inside corners, off-axis highs are heavily dismembered and ridge-perpendicular faulting is very prominent (Fig. 4).

At NTD outside corners, off-axis highs partly extend into the regions adjacent to the present-day NTD provinces. Off-axis highs bend into a NTD-related northeast-southwest trend (Fig. 6). In some cases, the inner walls of the off-axis highs are more oblique to the regional strike of the plate boundary than the present on-axis AVR tips.

4.3 Erosion and sedimentation

Sedimented surfaces appear smoother than their bare-rock counterparts with a moderate roughness and only minor inclination (Fig. 2 and 4). They predominantly cover magmatically and tectonically inactive areas, such as off-axis terrain, hence older crust.

Together with off-axis highs, sedimented plains cover most of the off-axis terrains of the Menez Gwen segment. They occur in elongated areas parallel to the ridge axis and deepen from 1600 m water depth at the segment center to up to 1900 m towards the segment ends (Fig. 6). Sedimented plains also occur on even surfaces with gentle slopes within active NTD provinces, interspersed with blocky terrain.

Terrain classified as talus occurs in patches with curved lower boundaries, dominantly on inward-facing slopes and fault scarps. These talus fans are small (less than 700 m across) and adjacent to the axial graben faults. Above these talus fans, strongly curved, short faults indicate the sources of the mass wasting (Fig. 5). The fans themselves are internally ruptured by concave-curved lineaments and faults, with steeper fans showing more ruptures indicating instabilities and recent movements. In contrast, off-axis fans are larger (more than 600 m across), have lower slope angles, and lack distinct break-off zones.

Within NTD provinces, talus material is associated with northeast-southwest-trending faults, especially on both large, inside corner fault scarps.

5. Discussion

Although the analysis of MBES data in terms of geological units is associated with a certain level of uncertainty, the systematic classification scheme presented here addresses the subjectivity in unit delineation by providing clear definitions of the parameters used to distinguish mapped units. Delineating unit boundaries will remain a subjective task until geometric and mathematical functions become capable of capturing the complexity of landforms (see discussion in Bishop et al., 2012).

Age relations derived from geological mapping allow the reconstruction of the spreading history with a significantly higher resolution than using magnetic anomalies (see Fig. 1).

Uncertainties in the mapping-derived ages include contributions from the resolution of the bathymetry data (30m pixel size) and errors on the spreading rates being used (± 0.2 mm/a, Argus et al., 2011), but also from our knowledge of the accretion mechanisms themselves. Extrusive volcanism can spread laterally and thus may potentially overprint older seafloor (Escartín et al., 2014). Furthermore, faults initiate at one side of the so-called 'dyke injection zone' (Buck et al., 2005, Behn and Ito, 2008); therefore, the width of the neo-volcanic zone results in an uncertainty of, on average, +/- 120 ka in calculated ages. Carbotte et al. (2006) attribute surface morphology on the intermediate-spreading Juan de Fuca Ridge to magma-induced deformation rather than episodic magmatic accretion. At Menez Gwen, subsurface dyking may contribute to the mapped morphology, but the observed accretion of the axial Menez Gwen volcano and of the AVR indicates focussing of extrusive magmatism at or near the ridge axis.

Nevertheless, the mapping derived age relations are still more precise than use of magnetic anomalies.

5.1. Age relations

Mapped crustal ages reach up to 2.5 Ma on the western ridge flank, and 3.5 Ma on the eastern counterpart. The average width of the neo-volcanic zone is 2400 m and, at a full-spreading rate of 20 mm/a, suggests that neo-volcanic activity occurred there over the past 120 ka (Fig. 6). As the neo-volcanic zone and the inner rift valley dissect the large Menez Gwen axial volcano, volcanism on this volcano consequently terminated about 120 ka ago. The flanks of the large Menez Gwen axial volcano cover crust of up to 800 ka for the base unit and of up to 540 ka for the upper cone unit.

The AVR, excluding the neo-volcanic zone, accumulated over a time period of, on average, 320 ka. Its across-axis width varies and is lowest at its tips and highest at the segment center, where it occupies up to 560 ka old crust (Fig. 6).

Off-axis, geological mapping reveals a series of sedimented plains and off-axis highs, for which opposite pairs can be identified on both sides of the spreading axis (Fig. 6). Sedimented plains that occur in between off-axis highs and also surrounding the current AVR show across-axis widths of around 2 km. These sedimented plains are interpreted as 200 ka-long periods of limited volcanic accretion, dominated by tectonic subsidence, mass wasting and sedimentation. Opposite pairs of off-axis highs resemble rifted halves of former AVRs, and reflect past periods of increased magmatic accretion (see 4.2.3). Comparing the spatial distribution of off-axis highs of the eastern and western ridge flank reveals asymmetries in the order of 100 ka. On the western ridge flank, off-axis high terrain occurs in four narrow ridges with an across-axis width ranging between 2 and 4 km, corresponding to volcanic periods of 200 to 400 ka (Fig. 6). In contrast, the eastern ridge flank shows two large areas of off-axis high terrain, each with an across-axis width of ca. 10 km, corresponding to volcanic periods of 1.000 ka. But, extensive fault zones with an overall throw of up to 300 m split both eastern off-axis highs in their middles resulting in four off-axis highs of 5 km across-axis width, suggesting two successive magmatic phases of 500 ka forming each large off-axis high terrain (off-axis high Ia and Ib, and off-axis high IIa and IIb, Fig. 6).

Extensive faults occur throughout the entire segment, predominantly marking the inward-facing boundary of off-axis highs like the outer rift walls (Fig. 6). The outer rift walls affect off-axis high-standing crust with an average age of 960 ka.

On the western ridge flank, prominent faults occur at distance intervals equivalent to time intervals, on average, of 400 ka. On the eastern ridge flank, most fault intervals are 500 ka, although a ca. 700 ka interval separates off-axis high Ib and IIa.

5.2. Segment-scale spreading processes

The geology and morphology of the Menez Gwen segment is controlled by both spreading-induced processes and NTD-related dynamics.

The overall smooth relief classifies the Menez Gwen segment as a ‘hotter segment’, following the nomenclature of Thibaud et al. (1998). The segment-scale extent of the axial volcanic ridge and the hourglass-shape of the neo-volcanic zone indicate recent, robust magma supply to the Menez Gwen spreading center (following Smith et al., 1995), resulting in significantly thickened crust underneath the center of the segment (Detrick et al., 1995).

The neo-volcanic zone is dominated by hummocky terrain, which is also observed in TOBI side-scan sonar data along the Menez Gwen axis (Parson et al., 2000). Following Yeo et al. (2012), hummocky terrain consists of lobate and pillow lava mounds, and topography-driven collapse talus. Dive observations from the Menez Gwen axial graben floor report predominantly pillow and lobate lavas (Ondreas et al., 1997, Fouquet et al., 1995).

On the ridge axis, fault length increases from the axial graben towards the NTDs, while fault density simultaneously decreases. This indicates a yield-strength dominated, hence rheology controlled along-axis stress accumulation, which is associated with focused magma and heat input (fault mode C following Behn et al., 2002). The off-axis high terrain shows a similar, although less pronounced fault distribution. Based on the assumption that main fault patterns develop close to the ridge axis, we interpret that the Menez Gwen segment has experienced only minor variations in spreading-related tectonic activity over time.

Despite the overall high fault density, only a few faults are observed in the center of the axial graben consistent with the occurrence of recent volcanic activity in the area (Fig. 5b). This correlates with visual observations during submersible dives that indicate only minor faulting and fissuring in this area, and the presence of young sheet flows (Ondreas et al., 1997, Fouquet et al., 1995).

Off-axis terrains lack signs of focused magma supply, such as fluid lava flow morphology, or large volcanic cones. Instead, mapped off-axis highs appear to be remnants of previous AVRs that were subsequently rifted apart. They occur in pairs on both sides of the ridge axis, only with a slight spatial asymmetry suggesting robust, periodic magmatic accretion at the Menez

Gwen spreading center over the past 3.5 Ma (Fig. 6). The average width of off-axis highs implies average accretion phase duration of ca. 320 ka. This is close to the average life span of AVRs elsewhere (~300 ka) estimated by Peirce and Sinha (2008).

Observed asymmetries between AVR remnants on either side of the present-day axis can be explained by alternating fault initiation at one side of the so-called 'dyke injection zone', on either side of the ridge axis (Buck et al., 2005, Behn and Ito, 2008). Considering this 'dyke injection zone' to coincide with the neo-volcanic zone, this results in a fault initiation zone of +/- 1.2 km away from the ridge axis. Observed asymmetries between off-axis high distribution on the Menez Gwen segment range within the corresponding +/- 120 ka variation. Despite asymmetric fault initiation, modelling for magmatically robust, slow-spreading crust results in an overall symmetric spreading pattern (Buck et al., 2005), as we see in the magnetic anomalies around the Menez Gwen segment (see Fig. 1; Cannat et al., 1999).

The along-axis extent of the former AVRs is greatest closest to the ridge axis – the present AVR is the longest of all. This apparently reflects an increase in the intensity of magmatic construction over the past 3.5 Ma at the Menez Gwen segment. Associated with this increase, more recent AVR-related dyke injections also affect the NTD provinces. Escartín et al. (2014) interpreted a large, ridge-parallel depression in the off-axis terrain of the nearby Lucky Strike segment as a propagating rift related to the Menez Gwen segment. This might indicate an along-axis propagation of tectonic deformation to the south accompanying widespread along-axis magmatic activity.

Near both NTDs, ridge-parallel faults accommodate large throws, which is typical for faults originating at segment ends (mode E faults, Behn et al., 2002). At NTD inside corners, large-throw faults and cross-cutting, NTD-parallel faults and graben structures contribute to a very high fault density. This coincides with missing inside-corner counterparts to outside-corner AVR halves of off-axis high terrain, suggesting NTD-related disruption.

Further off-axis, two long, ridge-perpendicular fault scarps with throws of 1000 m and 1500 m cut through inside-corner off-axis high terrain ('Large fault scarps', Fig. 6a). Their NTD-parallel orientation suggests NTD-related tectonic movements about 24 km away from the ridge axis, overprinting the original spreading-related morphology.

Within both NTDs, blocky terrain together with intense faulting, angular, and edged morphologies suggests on-going tectonic, brittle deformation. This correlates with observations in TOBI side-scan sonar imagery of Parson et al. (2000) of active fault planes and areas of exposed basement rocks. Detrick et al. (1995) explains an imaged negative gravity anomaly in the NTDs with thinned and/or cold crust. Cold crust would also explain the limited occurrence of volcanic units within the NTDs.

5.3. Focused magmatic activity

In contrast to the AVR-forming period between 3.5 Ma to 0.5 Ma ago, the past 500 ka of Menez Gwen spreading history are marked by voluminous, axial-volcano-forming magmatic accretion, supporting the existence of a robust magma reservoir at depth, whose presence has previously been suggested by Fouquet et al. (1995) and Marques et al. (2011). This magma chamber is probably the heat source powering the hydrothermal circulation at the Menez Gwen axial volcano. Delineating the units of the axial volcano shows a two-stage construction, with an older axial volcano base unit and a later-stage, cone unit. This conclusion is supported by outcropping massive flows (60 m flow thickness) at the bottom of the axial graben wall, overlain by a 240m-thick sequence of bedded volcanic ejecta (Fouquet et al., 1994). The massive lava flows suggest high effusion rate eruptions that would have had the potential to flow far into off-axis areas, covering existing morphology.

The axial volcano cone is superimposed on, and is therefore younger than, the axial volcano base, and presumably consists of bedded, volcanic ejecta. Ondreas et al. (1997) and Parson et al. (2000) interpreted 'mottled' textures in backscatter and TOBI side-scan data around the summit of the axial volcano as pyroclastic material and volcanic ejecta suggesting explosive volcanism. This coincides with the area identified in this study as the axial volcano cone (Fig. 5).

Both axial volcano units overprint the central part of the on-axis AVR, covering its characteristic, hummocky, volcanic morphology and the corresponding ridge-parallel fault pattern.

The Menez Gwen axial volcano base covers the entire across-axis width of the AVR. If interpreted in terms of spreading age, this would imply that they both have a similar accretion period (ca. 320 ka, see section 4.4.). The emplacement of the large axial volcano, however, clearly followed the AVR accretion and was presumably more rapid (as has also been suggested for the Lucky Strike axial volcano by Escartín et al., 2014). This apparent paradox is linked to the presence of both massive flows (suggesting large-scale burial of the surrounding, pre-existing seafloor) and bedded volcanic ejecta (which presumably spread well beyond their source) on the axial volcano.

Magmatic accretion at Menez Gwen developed from a typical, segment-scale AVR accretion that began approximately 450 ka ago, towards a segment-centered point source. Explosive volcanism was abundant during the last stage, before magmatic activity waned and tectonic dismemberment of the axial volcano became the dominant spreading process, starting about 120 ka ago. Melt focusing at the segment center and the formation of an axial volcano is also observed at other slow-spreading mid-ocean ridges, such as the neighbouring segments of Rifted Hills and Lucky Strike, or the southern equatorial MAR (Ondreas et al., 1999, Devey et al., 2010).

5.4. Crustal permeability and hydrothermal vent locations

Rifted, large axial volcanic highs appear to be prime targets for exploration for on-going hydrothermal activity (Fig. 7). This applies to the Menez Gwen and Lucky Strike segments of the northern Atlantic (Fig. 7a-b), but also to the southern Mid-Atlantic Ridge (Fig. 7c), where hydrothermal plume mapping identified the Merian vent site associated to a rifted axial volcanic high at 26°S (Petersen et al., 2013) following suggestions by Devey et al., (2010).

Besides the association with an axial volcanic high, both Menez Gwen vent fields occur in areas of very high fault densities ca. 2 km north and south of the drained lava lake at the axial graben center (Fig. 5a). In general, faulting contributes to the permeability of the upper crust and opens or sustains the pathways necessary for fluid circulation (Hearn et al., 2013, Andersen et al., 2017). The absence of large, deep-routing faults in the center of the axial graben potentially redirect rising hydrothermal fluids towards more permeable areas, according to models of hydrothermal fluid flow along slow-spreading ridges (Fouquet et al., 1997).

At Lucky Strike, hydrothermal activity clusters around the rim of a drained lava lake that is underlain by a magma chamber (Fouquet et al., 1995, Singh et al., 2006, Escartín et al., 2014, Fontaine et al., 2014).

The recent formation of the Menez Gwen cone in the north that hosts the vent field (Fig. 5) suggests an along-axis migration of magma and hence, a laterally dispersed heat source or magma chamber.

The Bubbylon vent field lies on the western axial graben wall that cuts through the large axial Menez Gwen volcano. The axial graben wall is a large, deep-rooting fault that are known to redirect fluids to sometimes far off-axis areas (e.g. Logatchev, TAG; McCaig et al., 2010; German et al., 2016). Redirection of fluids along the axial graben wall faults from a potential magma body at depth is supported by the detection of many additional hydrothermal bubble flairs along both axial graben walls (Dubilier et al., 2012).

5.5. Regional spreading processes

Since the formation of the Azores Volcanic Plateau 4 to 10 Ma ago (Cannat et al., 1999), the recent accretion of the Menez Gwen axial volcano has been an exceptional magmatic event, as equivalent features could not be identified in the off-axis areas.

Analyses of across-axis profiles and corresponding relative ages reveal regional correlations between the recent axial volcano accretion at Menez Gwen, and at the neighbouring Rifted Hills and Lucky Strike segments. Similar to the large Menez Gwen axial volcano, axial grabens rift the central edifices of the Rifted Hills and Lucky Strike segments and mark the time of waning magmatic activity. Emplacement of the main Lucky Strike axial volcano finished 200 to 150 ka ago (Escartín et al., 2014). Ondreas et al. (1997) report an axial graben width of about 2 km at Rifted Hills, which is similar to Menez Gwen's axial graben and would correspond to a decrease of magmatic activity at both segments some 100 ka ago. This may indicate that the period of increased magmatic activity forming the large central volcanoes was a regional phenomenon affecting three segments, and that on at least two of the segments the intensity of magmatism decreased at about the same time.

The occurrence of small volcanic cones on the ridge axes within the axial grabens at all three segments (which, in the case of Menez Gwen and Lucky Strike also host active hydrothermal systems) indicates that a period of focused, low-volume volcanism is presently affecting the entire region.

The volume of volcanic accretion decreases from Rifted Hills towards the Lucky Strike segment (toward the Azores Hotspot). The Rifted Hills axial volcano (22 km wide, 1200 m high; Ondreas et al., 1999) is larger than the Menez Gwen axial volcano (17 km wide, 800 m high, including the basal unit), while the Lucky Strike volcano is smallest (6 km wide, <400 m high; Fig. 7b). In addition, the Lucky Strike segment lacks an AVR, in contrast to Menez Gwen (Fig. 7a). At Rifted Hills, the ridge axis lies as shallow as at Menez Gwen (low resolution GMRT bathymetry, Fig. 1), and wide-spread areas of high acoustic reflectivity (Ondreas et al., 1999) suggest the presence of a segment-scale AVR.

The style of magmatism also differs at Lucky Strike when compared to Menez Gwen and Rifted Hills. Whereas volcanic ejecta form the summits of Menez Gwen and Rifted Hills, the Lucky

Strike main volcano consists of pillow and sheet flows (Ondreas et al., 1999, Escartín et al., 2014). This may relate to the deeper water depth at Lucky Strike.

6. Conclusions

Systematic geomorphologic analysis and geological interpretation of ship-based multibeam and acoustic backscatter data enabled the production of a geological map of the entire Menez Gwen segment and of the adjacent NTDs.

(1) This study uses the geological map of an entire slow-spreading mid-ocean ridge segment to provide a detailed analysis of the segment's spreading history at significantly higher resolution than previous interpretations using magnetic anomalies.

(2) We interpret that magmatic activity of the Menez Gwen segment occurs in periods of increased volcanic accretion lasting for around 300 ka and happening with a frequency of 300 to 500 ka. Asymmetries between both ridge flanks are within the dimensions of the neovolcanic zone and the distribution of fault initiation.

(3) At Menez Gwen, the most recent magmatic phase was apparently exceptionally intense and was associated with axial volcanic ridge accretion that i) extends beyond the initial bounds of the segment, and ii) developed into focused magmatism forming a segment-centred large axial volcano with late-stage, explosive volcanism.

(4) A (cooling) magma chamber at depth from this most recent stage is potentially driving hydrothermal activity at Menez Gwen.

(5) Hydrothermal vent locations are determined by an interplay of heat supply and permeability variations in the upper crust as derived from the fault pattern. Both hydrothermal vent fields are located within 2 km off the segment center and are associated with a permeability contrast.

(6) Venting at Bubblyon is unfocused and fed by fluids redirected along the deep-routing axial graben faults.

(7) Termination of the intense magmatic phase about 120 ka ago resulted in rifting and break up of both, the axial volcanic ridge and the large Menez Gwen axial volcano. This break up of cooling magmatic crust is accompanied by hydrothermal activity.

(8) These periods of enhanced magmatic activity and tectonism are regional phenomena affecting the Menez Gwen, Lucky Strike, and Rifted Hills segments at nearly the same time.

7. Data availability

The multibeam echosounder data used in this study are available from the open access library PANGAEA (https://doi.pangaea.de/10.1594/PANGAEA.819963; Dubilier, 2013).

Acknowledgements

This work benefited from the MBES processing experience of C. dos Santos Ferreira, and constructive comments by N. Augustin and I.A. Yeo. We thank William Chadwick and an anonymous reviewer for their constructive and careful review.

Formatting of funding sources

The cruise M82/3 was funded through the Deutsche Forschungs-Gemeinschaft (DFG). This research project was supported from GEOMAR – Helmholtz Center for Ocean Research Kiel, and the development of mapping criteria has been funded through the WTZ China – OASIS project (03F0724A) in the framework of MARE:N – coastal, marine and polar research for sustainability.

References:

Allerton, S., Murton, B.J., Searle, R.C., Jones, M., 1995. Extensional Faulting and Segmentation of the Mid-Atlantic Ridge North of the Kane Fracture Zone (24°00’N to 24°40’N). *Marine Geophysical Researches* 17, 37-61.

Andersen, C., Theissen-Krah, S., Hannington, M., Rupke, L., Petersen, S., 2017. Faulting and off-axis submarine massive sulfide accumulation at slow spreading mid-ocean ridges:

A numerical modeling perspective. *Geochemistry, Geophysics, Geosystems* 18, 2305–2320. doi:10.1002/2017GC006880.

Anderson, M.O., Chadwick, W.W., Hannington, M.D., Merle, S.G., Resing, J.A., Baker, E.T., Butterfield, D.A., Walker, S.L., Augustin, N., 2017. Geological interpretation of volcanism and segmentation of the Mariana back-arc spreading center between 12.7°N and 18.3°N: GEOLOGY OF THE MARIANA BACK-ARC. *Geochemistry, Geophysics, Geosystems* 18, 2240–2274. https://doi.org/10.1002/2017GC006813.

Anderson, M. O., Hannington, M. D., Haase, K., Schwarz-Schampera, U., Augustin, N., McConachy, T. F. und Allen, K., 2016. Tectonic focusing of voluminous basaltic eruptions in magma-deficient backarc rifts. *Earth and Planetary Science Letters* 440, 43-55. http://dx.doi.org/10.1016/j.epsl.2016.02.002.

Anderson, M. O., Chadwick, W. W., Hannington, M. D., Merle, S. G., Resing, J. A., Baker, E. T., Butterfield, D. A., Walker, S. L. und Augustin, N., 2017. Geological interpretation of volcanism and segmentation of the Mariana back-arc spreading center between 12.7°N and 18.3°N. *Geochemistry, Geophysics, Geosystems* 18(6), 2240-2274. http://dx.doi.org/10.1002/2017GC006813.

Argus, D.F., Gordon, R.G., DeMets, C., 2011. Geologically current motion of 56 plates relative to the no-net-rotation reference frame. *Geochemistry, Geophysics, Geosystems* 12(11). http://dx.doi.org/10.1029/2011GC003751.

Baker, E. T., German, C.R., 2004. On the Global Distribution of Hydrothermal Vent Fields, in: German, C.R., Lin, J., Parson, L.M. (Eds.), Mid-Ocean Ridges. American Geophysical Union, Washington, D. C. http://dx.doi.org/10.1029/148GM10.

Baker, E. T., 2017. Exploring the ocean for hydrothermal venting: New techniques, new discoveries, new insights. *Ore Geology Reviews* 86, 55-69.

Beaulieu, S.E., Baker, E.T., German, C.R., 2013. An authoritative global database for active submarine hydrothermal vent fields. *Geochemistry, Geophysics, Geosystems* 14(11), 4892–4905.

Behn, M.D, Lin, J., Zuber, M.T., 2002. Mechanisms of normal fault development at mid-ocean ridges. *Journal of Geophysical Research* 107(B4), 2083, doi:10.1029/2001JB000503.

Behn, M.D., Ito, G., 2008. Magmatic and tectonic extension at mid-ocean ridges: 1. Controls on fault characteristics. *Geochemistry, Geophysics, Geosystems* 9(8). http://dx.doi.org/10.1029/2008GC001965.

Bishop, M.P., James, L.A., Shroder Jr., J.F., Walsh, S.J., 2012. Geospatial technologies and digital geomorphological mapping: Concepts, issues and research. *Geomorphology* 137, 5-26.

Bogdanov, Y.A., Lein, A.Y., Sagalevich, A.M., 2005. Chemical Composition of the Hydrothermal Deposits of the Menez Gwen Vent Field (Mid-Atlantic Ridge). *Oceanology* 45(6), 849–856.

Brown, L., 2010. A new technique for depicting terrain relief [abstract]. In: NACIS Annual Meeting, 2010 Oct 13-17, St. Petersburg, Florida.

Borowski, C., Meinecke, G., Meyer, V., Nowald, N., Renken, J., Ruhland, G., Wendt, J., Wintersteller, P., Thal, J., 2010. Cruise Report MENEZKART RV POSEIDON Cruise No. 402, 1–32.

Buck, W.R., Lavier, L.L., Poliakov, A.N.B., 2005. Modes of faulting at mid-ocean ridges. *Nature* 434, 719–723.

Canales, J.P., Sohn, R.A., deMartin, B.J., 2007. Crustal structure of the Trans-Atlantic Geotraverse (TAG) segment (Mid-Atlantic Ridge, 26°10’N): Implications for the nature of hydrothermal circulation and detachment faulting at slow spreading ridges. *Geochemistry, Geophysics, Geosystems* 8 (8).

Cannat, M., Briais, A., Deplus, C., Escartín, J., Georgen, J., Lin, J., Mercouriev, S., Meyzen, C., Muller, M., Pouliquen, G., Rabain, A., da Silva, P., 1999. Mid-Atlantic Ridge–Azores hotspot interactions: along-axis migration of a hotspot-derived event of enhanced magmatism 10 to 4 Ma ago. *Earth and Planetary Science Letters* 173, 257–269.

Carbotte, S.M., Detrick, R.S., Harding, A., Canales, J.P., Babcock, J., Kent, G., Ark, E.V., Nedimovic, M., Diebold, J., 2006. Rift topography linked to magmatism at the intermediate spreading Juan de Fuca Ridge. Geology 34, 209. https://doi.org/10.1130/G21969.1

Charlou, J.L., Donval, J.P., Douville, E., Jean-Baptiste, P., Radford-Knoery, J., Fouquet, Y., Dapoigny, A., Stievenard, M., 2000. Compared geochemical signatures and the evolution of Menez Gwen (37°50’N) and Lucky Strike (37°17'N) hydrothermal fluids, south of the Azores Triple Junction on the Mid-Atlantic Ridge. *Chemical Geology* 171, 49–75.

Clague, D. A., J. B. Paduan, D. W. Caress, W. W. Chadwick Jr., M. L. Saout, B. Dreyer, and R. Portner, 2017. High-resolution AUV mapping and targeted ROV observations of three historical lava flows at Axial Seamount. *Oceanography* 30(4), 82-99, doi:10.5670/oceanog.2017.426.

Clague, D. a., Moore, J.G. & Reynolds, J.R., 2000. Formation of submarine flat-topped volcanic cones in Hawai’i. *Bulletin of Volcanology* 62(3), 214–233.

DeMets, C., Gordon, R.G., Argus, D.F., 2010. Geologically current plate motions. *Geophysical Journal International* 181(1), 1–80.

Detrick, R.S., Needham, H.D., Renard, V., 1995. Gravity anomalies and crustal thickness variations along the Mid-Atlantic Ridge between 33°N and 40°N. *Journal of Geophysical Research* 100(B3), 3767–3787.

Devey, C.W., German, C.R., Haase, K.M., Lackschewitz, K.S., Melchert, B., Connelly, D.P., 2010. The Relationships Between Volcanism, Tectonism, and Hydrothermal Activity on the Southern Equatorial Mid-Atlantic Ridge, in: Rona, P.A., Devey, C.W., Dyment, J., Murton, B.J. (Eds.), Diversity of Hydrothermal Systems on Slow Spreading Ocean Ridges. American Geophysical Union, Washington, D. C., 133-152. http://dx.doi.org/10.1029/2008GM000756.

Dosso, L., Bougault, H., Langmuir, C., Bollinger, C., Bonnier, O., Etoubleau, J., 1999. The age and distribution of mantle heterogeneity along the Mid-Atlantic Ridge (31–41°N). *Earth and Planetary Science Letters* 170(3), 269–286.

Dubilier, N., and the M82/3 scientific party, 2012. Interdisciplinary Geological, Chemical and Biological Studies at the Menez Gwen Hydrothermal Vent Field Mid-Atlantic Ridge, at 37°50’N. Meteor-Reports, No. 82, Leg 3, 1–73.

Dubilier, N., 2013. Swath sonar multibeam EM122 bathymetry during METEOR cruise M82/3 with links to raw data files of bathymetry and water column information. *Max-Planck-Institut für Marine Mikrobiologie, PANGAEA*. https://doi.org/10.1594/PANGAEA.819963.

Eason, D.E., Dunn, R.A., Canales, J.P., Sohn, R.A., 2016. Segment-scale variations in seafloor volcanic and tectonic processes from multibeam sonar imaging, Mid-Atlantic Ridge Rainbow region (35°45’-36°35’N). *Geochemistry, Geophysics, Geosystems* 17. http://dx.doi.org/10.1002/2016GC006433.

Escartín, J., Cannat, M., Fornari, Pouliquen, G., Rabain, A., Lin, J. 2001. Crustal thickness of V-shaped ridges south of the Azores: Interaction of the Mid-Atlantic Ridge (36°-39°N) and the Azores hotspot. *Journal of Geophysical Research* 106(B10), 21,719-21,735.

Escartín, J., Soule, S.A., Cannat, M., Fornari, D.J., Düsünür, D., Garcia, R., 2014. Lucky Strike seamount: Implications for the emplacement and rifting of segment-centered volcanoes at slow spreading mid-ocean ridges. *Geochemistry, Geophysics, Geosystems* 15, 4157-4179. http://dx.doi.org/10.1002/2014GC005477.

Escartín, J., Barreyre, T., Cannat, M., Garcia, R., Gracias, N., Deschamps, A. Salocchi, A., Sarradin, P.-M., Ballu, V., 2015. Hydrothermal activity along the slow-spreading Lucky Strike ridge segment (Mid-Atlantic Ridge): Distribution, heatflux and geological controls. *Earth and Planetary Science Letters* 431, 173-185. http://dx.doi.org/10.1016/j.epsl.2015.09.025.

Escartín, J., Mével, C., Petersen, S., Bonnemains, D., Cannat, M., Andreani, M., Augustin, N., Bezos, A., Chavagnac, V., Choi, Y., Godard, M., Haaga, K., Hamelin, C., Ildefonse, B., Jamieson, J., John, B., Leleu, T., MacLeod, C. J., Massot-Campos, M., Nomikou, P., Olive, J. A., Paquet, M., Rommevaux, C., Rothenbeck, M., Steinfuhrer, A., Tominaga, M., Triebe, L., Campos, R., Gracias, N. und Garcia, R., 2017. Tectonic structure, evolution, and the nature of oceanic core complexes and their detachment fault zones (13°20°N and 13°30'N, Mid Atlantic Ridge). *Geochemistry, Geophysics, Geosystems* 18 (4), 1451-1482. http://dx.doi.org/10.1002/2016GC006775.

Fontaine, F.J., Cannat, M., Escartín, J., Crawford, W.C., 2014. Along-axis hydrothermal flow at the axis of slow spreading Mid-Ocean Ridges: Insights from numerical models of the Lucky Strike vent field (MAR). *Geochemistry, Geophysics, Geosystems* 15, 2918-2931. http://dx.doi.org/10.1002/2014GC005372.

Fouquet, Y., Charlou, J.-L., Costa, I., Donval, J.-P., Radford-Knoery, J., Pelle, H., Ondreas, H., Lourenco, N, Segonzac, M., Tivey, M.K., 1994. A Detailed Study of the Lucky Strike Hydrothermal Site and Discovery of a New Hydrothermal Site: Menez Gwen; Preliminary Results of the DIVA1 Cruise (5-29 May, 1994). *InterRidge News* 3(2), 14–17.

Fouquet, Y., Ondreas, H., Charlou, J.-L., Donval, J.-P., Radford-Knoery, J., 1995. Atlantic lava lakes and hot vents. *Nature* 377(6546), 201–201.

Fouquet, Y., 1997. Where are the large hydrothermal sulphide deposits in the oceans? Philosophical Transactions of the Royal Society of London. Series A: Mathematical, Physical and Engineering Sciences 355, 15. https://doi.org/10.1098/rsta.1997.0015.

German, C.R., Parson, L.M., HEAT Scientific Team, 1995. Hydrothermal exploration near the Azores Triple Junction: tectonic control of venting at slow-spreading ridges? *Earth and Planetary Science Letters* 138(1-4), 93–104.

German, C.R., Parson, L., 1998. Distributions of hydrothermal activity along the Mid-Atlantic Ridge: interplay of magmatic and tectonic controls. *Earth and Planetary Science Letters* 160(3-4), 327–341.

German, C.R., Petersen, S., Hannington, M.D., 2016. Hydrothermal exploration of mid-ocean ridges: Where might the largest sulfide deposits be forming? *Chemical Geology* 420, 114–126.

Gràcia, E., Charlou, J.L., Radford-Knoery, J., Parson, L.M., 2000. Non-transform offsets along the Mid-Atlantic Ridge south of the Azores (38°N-34°N): ultramafic exposures and hosting of hydrothermal vents. *Earth and Planetary Science Letters* 177, 89–103.

Grosse, P., van Wyk de Vries, B., Euillades, P.A., Kervyn, M., Petrinovic, I.A., 2012. Systematic morphometric characterization of volcanic edifices using digital elevation models. *Geomorphology* 136(1), 114–131.

Hannington, M.D., Jonasson, I.R., Herzig, P.M., Petersen, S., 1995. Physical and Chemical Processes of Seafloor Mineralization at Mid-Ocean Ridges, in: Humphris, S.E., Zierenberg, R.A., Mullineaux, L.S., Thomson, R.E., (Eds.), Seafloor Hydrothermal Systems: Physical, Chemical, Biological, and Geological Interactions. *Geophysical Monograph* 91, American Geophysical Union, 115–157.

Hannington, M.D., de Ronde, C.E.L., Petersen, S., 2005. Sea-Floor Tectonics and Submarine Hydrothermal Systems. Economic Geology 100th Anniversary Volume, 111-141.

Harris, P.T., Macmillan-Lawler, M., Rupp, J., Baker, E.K., 2014. Geomorphology of the oceans. Marine Geology, Vol. 352, pp. 4–24.

Hearn, C. K., Homola, K. L., and Johnson, H. P., 2013. Surficial permeability of the axial valley seafloor: Endeavour Segment, Juan de Fuca Ridge. *Geochemistry, Geophysics, Geosystems* 14, 3409–3424.

Lein, A.Y., Bogdanov, Y.A., Maslennikov, V.V., Syaoli Li, Ulyanova, N.V., Maslennicova, S.P., Ulyanov, A.A., 2010. Sulfide minerals in the Menez Gwen nonmetallic hydrothermal field (Mid-Atlantic Ridge). *Lithology and Mineral Resources* 45(4), 305–323.

Luis, J.F., Miranda, J.M., Galdeano, A., Patriat, P., Rossignol, J.C., Victor, L.A.M., 1994. The Azores triple junction evolution since 10 Ma from an aeromagnetic survey of the Mid-Altantic Ridge. Earth and Planetary Science Letters 125, 439-459.

Marcon, Y., Sahling, H., Borowski, C., dos Santos Ferreira, C., Thal, J., Bohrmann, G., 2013. Megafaunal distribution and assessment of total methane and sulfide consumption by mussel beds at Menez Gwen hydrothermal vent, based on geo-referenced photomosaics. *Deep Sea Research Part I: Oceanographic Research Papers* 75, 93–109.

Marques, A.F.A., Scott, S.D., Gorton, M.P., Barriga, F.J.A.S., Fouquet, Y., 2009. Pre-eruption history of enriched MORB from the Menez Gwen (37°50′N) and Lucky Strike (37°17′N) hydrothermal systems, Mid-Atlantic Ridge. *Lithos* 112(1-2), 18–39.

Marques, A.F.A., Scott, S.D., Guillong, M., 2011. Magmatic degassing of ore-metals at the Menez Gwen: Input from the Azores plume into an active Mid-Atlantic Ridge seafloor hydrothermal system. *Earth and Planetary Science Letters* 310(1-2), 145–160.

McAllister, E., Cann, J.R., 1996. Initiation and evolution of boundary-wall faults along the Mid-Atlantic Ridge, 25-29°N. *Geological Society, London, Special Publications* v.118, 29-48. http://dx.doi.org/10.1144/GSL.SP.1996.118.01.03.

McCaig, A.M., Delacour, A., Fallick, A.E., Castelain, T., Früh-Green, G.L., 2010. Detachment Fault Control on Hydrothermal Circulation Systems: Interpreting the Subsurface Beneath the TAG Hydrothermal Field Using the Isotopic and Geological Evolution of Oceanic Core Complexes in the Atlantic. *Geophysical Monograph Series* 188. http://dx.doi.org/10.1029/2008GM000729.

McClinton, T., White, S.M., Colman, A., Sinton, J.M., 2013. Reconstructing lava flow emplacement processes at the hot spot-affected Galápagos Spreading Center, 95°W and 92°W. *Geochemistry, Geophysics, Geosystems* 14(8). http://dx.doi.org/10.1002/ggge.20157.

Minár, J., Evans, I.S., 2008. Elemantary forms for land surface segmentation: The theoretical basis of terrain analysis and geomorphological mapping. *Geomorphology* 95, 236-259.

Ondréas, H., Fouquet, Y., Voisset, M., 1997. Detailed Study of Three Contiguous Segments of the Mid-Atlantic Ridge, South of the Azores (37°N to 38°30'N), Using Acoustic Imaging Coupled with Submersible Observations. *Marine Geophysical Researches* 19, 231–255.

Parson, L., Gràcia, E., Coller, D., German, C., Needham, D., 2000. Second-order segmentation; the relationship between volcanism and tectonism at the MAR, 38°N–35°40′N. *Earth and Planetary Science Letters* 178(3-4), 231–251.

Peirce, C., Sinha, M.C., 2008. Life and death of axial volcanic ridges: Segmentation and crustal accretion at the Reykjanes Ridge. *Earth and Planetary Science Letters* 274(1-2), 112-120.

Petersen, S., Devey, C.W., Walter, M., Jamieson, J.W., Yeo, I., Nakamura, K., Rothenbeck, M., Steinführer, A., Triebe, L., 2013. AUV-based long-range exploration for hydrothermal activity between 13°-33°S along the Southern Mid- Atlantic Ridge. Proceedings of the 42nd Underwater Mining Institute, Rio de Janeiro, 1–6.

Reston, T., Weinrebe, W., Grevemeyer, I., Flueh, E.R., Mitchell, N.C., Kirstein, L., Kopp, C., Kopp, H., participants of Meteor 47/2, 2002. A rifted inside corner massif on the Mid-Atlantic Ridge at 5°S. *Earth and Planetary Science Letters* 200, 255–269.

Ryan, W.B.F., S.M. Carbotte, J.O. Coplan, S. O'Hara, A. Melkonian, R. Arko, R.A. Weissel, V. Ferrini, A. Goodwillie, F. Nitsche, J. Bonczkowski, and R. Zemsky, 2009. Global Multi-Resolution Topography synthesis. *Geochemistry, Geophysics, Geosystems* 10. http://dx.doi.org/10.1029/2008GC002332.

Searle, R.C., Murton, B.J., Achenbach, K., LeBas, T., Tivey, M., Yeo, I., Cormier, M.H., Carlut, J., Ferreira, P., Mallows, C., Morris, K., Schroth, N., van Calsteren, P., Walters, C., 2010. Structure and development of an axial volcanic ridge: Mid-Atlantic Ridge, 45°N. *Earth and Planetary Science Letters* 299, 228-241.

Singh, S.C., Crawford, W.C., Carton, H., Seher, T., Combier, V., Cannat, M., Canales, J.P., Düsünür, D., Escartín, J., Miranda, J.M., 2006. Discovery of a magma chamber and faults beneath a Mid-Atlantic Ridge hydrothermal field. *Nature* 442(7106), 1029–32.

Smith, D.K., Cann, J.R., Dougherty, M.E., Lin, J., Spencer, S., MacLeod, C., Keeton, J., McAllister, E., Brooks, B., Pascoe, R., Robertson, W., 1995. Mid-Atlantic Ridge volcanism from deep-towed side-scan sonar images, 25°-29°N. *Journal of Volcanology and Geothermal Research* 67, 233-262.

Thibaud, R., Gente, P., Maia, M., 1998. A systematic analysis of the Mid-Atlantic Ridge morphology and gravity between 15°N and 40°N: Constraints on the thermal structure. *Journal of Geophysical Research* 103(B10), 24,223-24,243.

Yang, T., Shen, Y., van der Lee, S., Solomon, S.C., Hung, S.-H., 2006. Upper mantle structure beneath the Azores hotspot from finite-frequency seismic tomography. *Earth and Planetary Science Letters* 250(1-2), 11-26. http://dx.doi.org/10.1016/j.epsl.2006.07.031.

Yeo, I., Searle, R.C., Achenbach, K.L., LeBas, T.P., Murton, B.J., 2012. Eruptive hummocks: Building blocks of the upper ocean crust. *Geology* 40(1), 91–94. http://dx.doi.org/10.1130/G31892.1.

Yeo, I.A., Devey, C.W., LeBas, T.P., Augustin, N., Steinführer, A., 2016. Segment-scale volcanic episodicity: Evidence from the North Kolbeinsey Ridge, Atlantic. *Earth and Planetary Science Letters* 439, 81–87. http://dx.doi.org/10.1016/j.epsl.2016.01.029.

Figure Captions

Figure 1. GMRT bathymetry (Ryan et al., 2009) around the Menez Gwen segment at 37°50'N on the Mid-Atlantic Ridge (MAR). Inset shows location of the Menez Gwen segment on the MAR south of the Azores. The MAR spreading axis (red lines) is offset by right-stepping non-transform discontinuities (NTD), characterized by bathymetric deeps. The black line outlines the area covered by multibeam echosounder data acquired during *Meteor* cruise M82/3 and analysed in this study. Stars mark confirmed hydrothermal vent sites. Yellow-white colouring (referring to water depths shallower than 1700 m) highlights the axial volcanos of the Menez Gwen segment, and of the neighbouring segments Rifted Hills and Lucky Strike. The colouring also emphasizes the shallow Azores Volcanic Plateau that formed between 4 and 10 Ma ago and has been rifted since then (magnetic anomalies 3 and 5, after Cannat et al., 1999).

Figure 2. Colour-shaded, analysed DEM (A) and corresponding MBES backscatter mosaic with major geological features (B). A) Coloured, slope-shaded DEM derived from processed EM122 bathymetry from cruise M82/3 with 30 m spatial resolution (black outline) and 10 m resolution (outlined in grey, see Fig. 5 for more detail). Stars indicate the two known active vent sites Menez Gwen in about 800 m, and Bubbylon in ca. 1000 m water depth. Both sites are located in the axial graben, which is part of the inner rift valley, rifting the large Menez Gwen axial volcano (see B) and the surrounding axial volcanic ridge (AVR, outlined by dotted yellow line). B) Backscatter mosaic with relatively high intensities in white and low backscatter

intensities in black. As in A, the dotted yellow line marks the AVR, which is characterized by generally high backscatter intensities. The light green outlines the highest backscatter intensities associated with the neo-volcanic zone and young, bare rock surfaces. The darker green outline marks the (half-) cone-shaped flanks of the large Menez Gwen axial volcano, which show moderate backscatter intensities, presumably due to both, their steeper slopes and their volcanoclastic composition.

Figure 3. Plate with map examples of analysed relief-shaded digital elevation model (A, D, G; terrain texture shading algorithm 'TTS', following Brown et al., 2010), backscatter mosaics (B, E, H) and the resulting outlines of mapped geological units with the shaded relief in the background (C, F, I). Mapped faults and lineaments are not displayed for clarity. The examples demonstrate the geomorphological and acoustic mapping criteria of the most common terrain units, including volcanos and off-axis high terrain (A–C), sedimented plains and lava flows (D–F), and hummocky and smooth hummocky terrain (G–I). The backscatter mosaic mainly assists geomorphological analyses, but in some cases is used to define subclasses, e.g., distinguishing between sedimented plain and lava flow (D–F).

Figure 4. Fault density map (A) and geological map (B) of the Menez Gwen segment, based on analysis of the 30 m DEM. A) Fault density map (blue shading), calculated as kernel density from the digitized faults (thin, black lines) with a grid size of 100 m and a 2 km search radius. It highlights the most faulted, tectonized areas in dark blue. Highest fault densities are found around the vent sites in the axial graben, surrounding a low-density area correlating with the area around the drained lava lake. High fault densities occur also at the inside corners towards bounding NTDs, where ridge-perpendicular faulting intersects with axis-parallel faulting. Thicker, dotted black lines mark the fault zones forming the inner and outer rift walls with overall throws of 100-400 m. Volcanos are indicated to show the distribution of focused volcanic activity in the neo-volcanic zone (see also B). B) Geological map of the Menez Gwen segment, based on systematic classification of the MBES derived 30 m DEM and according

backscatter intensities (Fig. 2) following criteria summarised in Table 1. The ridge axis is dominated by the axial volcanic ridge (AVR) consisting of (smooth) hummocky terrain, which is overprinted by the large axial Menez Gwen volcano. Both, the large axial volcano and the AVR, are cut by the inner rift valley bounding the neo-volcanic zone. Off-axis, the segment shows a sequence of elongated, axis-parallel sedimented plains and off-axis highs. NTD areas are dominated by blocky terrain.

Figure 5. Colour-shaded DEM with 10 m spatial resolution (A) and derived geological map (B) of the large axial Menez Gwen volcano rifted by the axial graben. A) DEM of the processed EM710 bathymetry shaded using the slope map from 0° (white) to 30° (black). The EM120 derived 30 m DEM without any shading is in the background. Green lines mark the basal (light green) and cone-shaped top unit (dark green) of the large Menez Gwen axial volcano (see also B). The purple outline is the flat seafloor and very high backscatter intensities characterizing the drained lava lake, observed during submersible dives (Fouquet et al., 1995, Ondreas et al., 1999). While the drained lava lake is located at the deepest part of the axial graben, both vent fields are associated to relative highs and high fault densities (see also B and Fig. 4A). B) Geological map of the same area as in A. Talus fans, associated with curved, short faults, occupy large parts of the axial graben walls and narrowing the neo-volcanic zone. Dive observations report outcropping massive flows at the bottom of the western axial graben wall, overlain by bedded pyroclastics (Fouquet et al., 1994). The Menez Gwen vent field lies on faults cutting through the young Menez Gwen volcano. Bubbylon is associated to talus, which is confirmed by dive observations (Dubilier et al., 2012).

Figure 6. A) Geologic map with profile lines corresponding to the cross sections presented in B. B) Axis-perpendicular cross sections (vertical exaggeration of 4) through the Menez Gwen segment from west (left) to east (right), and north (A–A’) to south (D–D’). Colors refer to the mapped terrain units in A. Dashed lines connect major fault zones (black) and the ridge axis (red), which is considered to reflect crust of zero age. Grey shading highlights relatively

elevated areas of off-axis high terrain interpreted to reflect periods of increased magmatic activity. On the western ridge flank, magmatic periods lasted 200 to 400 ka, while on the eastern flanks, the distribution of off-axis highs suggests two successive magmatic periods of 500 ka each (off-axis high Ia and Ib, and IIa and b). The dark grey shading marks the on-axis axial volcanic ridge (AVR) reflecting a recent phase of high magmatic accretion at the Menez Gwen segment. At the segment center, the AVR affects crust of up to 560 ka and is overprinted by the large Menez Gwen axial volcano (profiles B–B' and C–C').

Figure 7. Ship-based MBES derived DEMs of three axial volcanos hosting active hydrothermal venting: A) the Menez Gwen segment with the vent fields Menez Gwen and Bubbylon, B) the Lucky Strike segment hosting the on-axis Lucky Strike vent field and the off-axis Capelinhos vent site, and C) the Merian vent field at 26°S on the slow-spreading, southern equatorial MAR. The dark green lines mark the extent of the axial volcanos and the purple areas the drained lava lakes (Lucky Strike volcano and drained lava lake outline after Escartín et al., 2014). The dashed black line indicates the axial magma chamber found underneath Lucky Strike (after Singh et al., 2006).

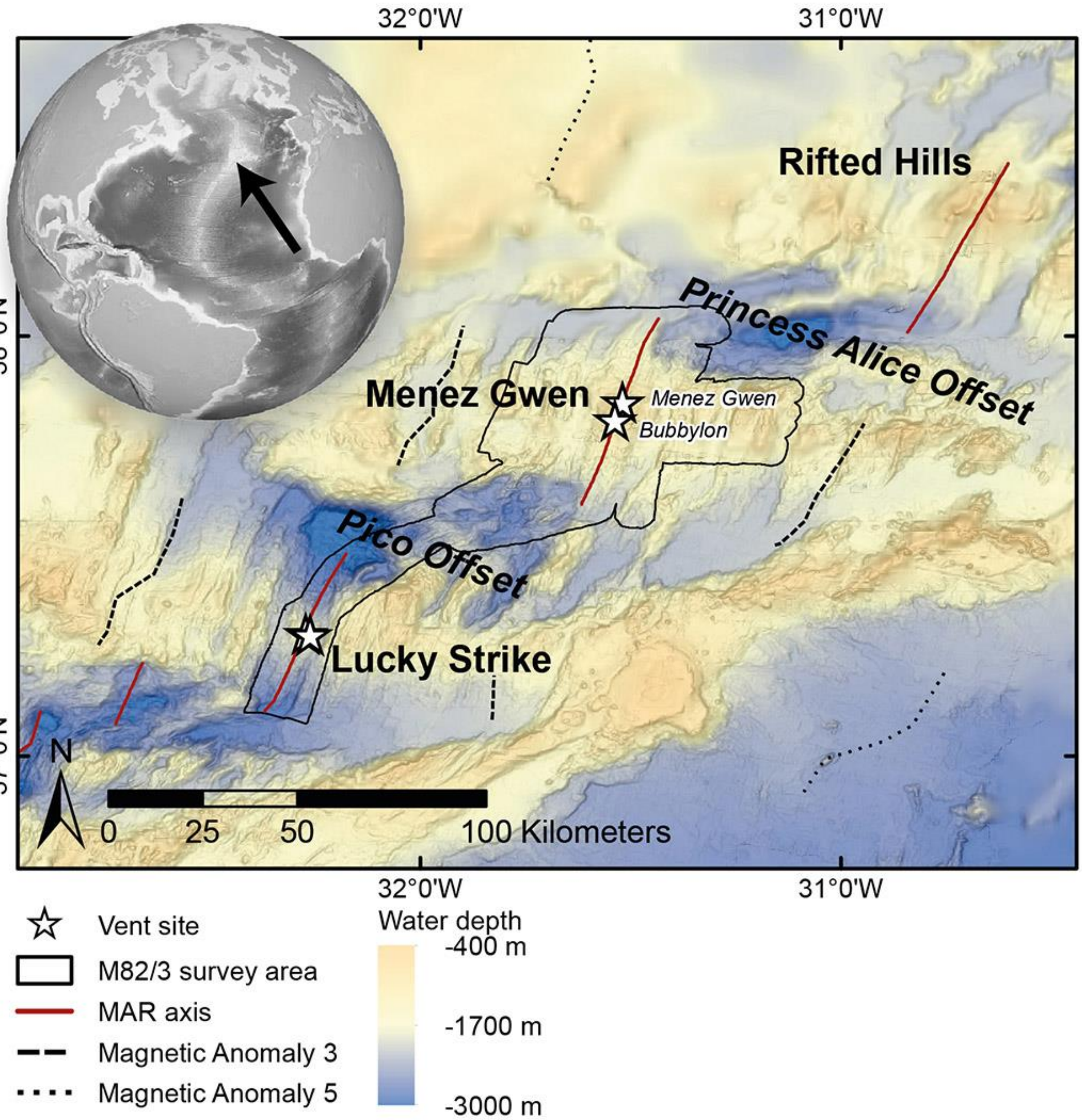
32°0'W
31°0'W
38°0'N
37°0'N
Rifted Hills
Princess Alice Offset
Menez Gwen
Menez Gwen
Bubbylon
Pico Offset
Lucky Strike
N
0 25 50 100 Kilometers
Vent site
M82/3 survey area
MAR axis
Magnetic Anomaly 3
Magnetic Anomaly 5
Water depth
-400 m
-1700 m
-3000 m

928

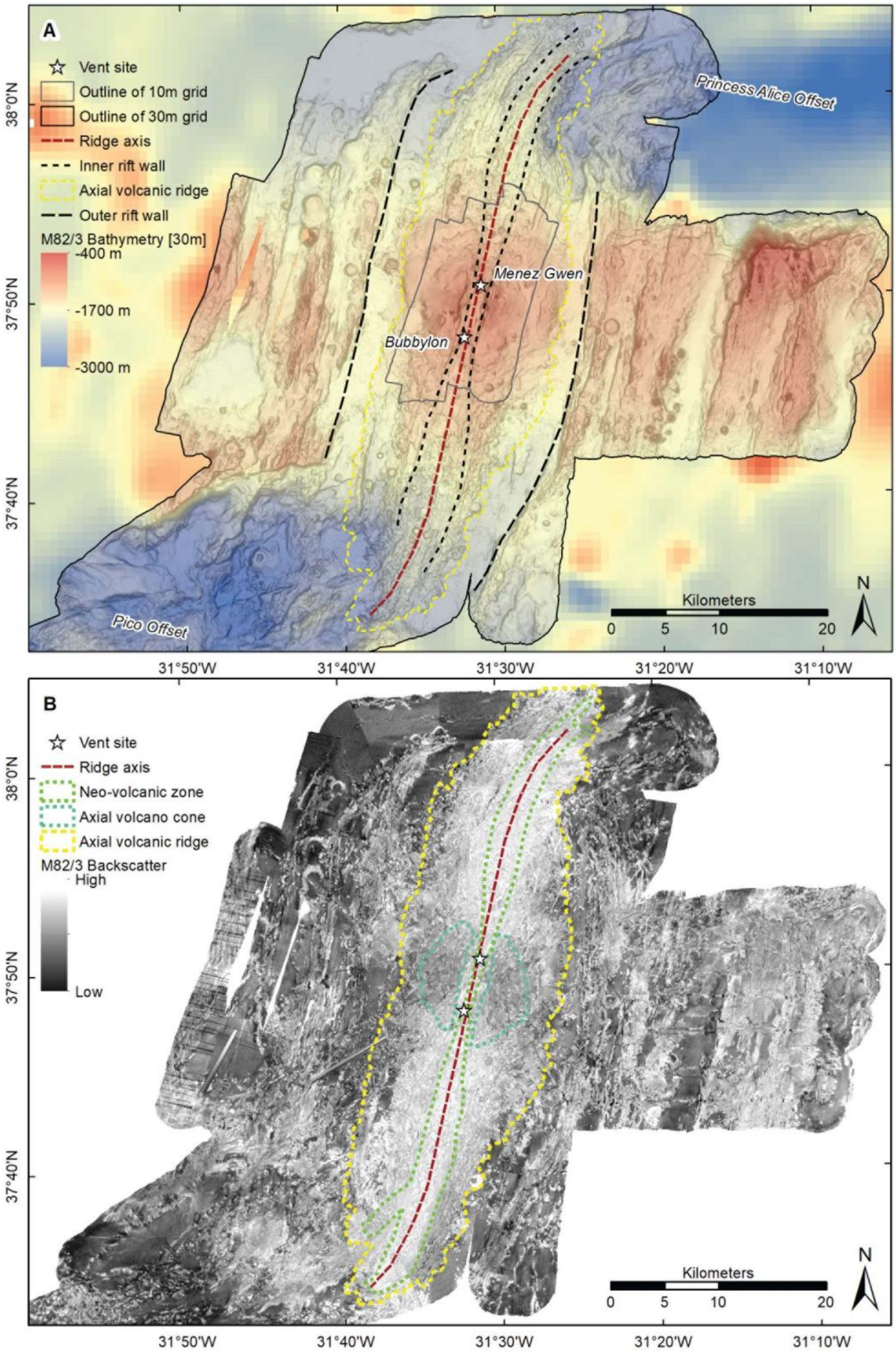
A
Vent site
Outline of 10m grid
Outline of 30m grid
Ridge axis
Inner rift wall
Axial volcanic ridge
Outer rift wall
M82/3 Bathymetry [30m]
-400 m
-1700 m
-3000 m
Princess Alice Offset
Menez Gwen
Bubbylon
Pico Offset
Kilometers
0
5
10
20
N
38°0'N
37°50'N
37°40'N
31°50'W
31°40'W
31°30'W
31°20'W
31°10'W
B
Vent site
Ridge axis
Neo-volcanic zone
Axial volcano cone
Axial volcanic ridge
M82/3 Backscatter
High
Low
Kilometers
0
5
10
20
N
38°0'N
37°50'N
37°40'N
31°50'W
31°40'W
31°30'W
31°20'W
31°10'W

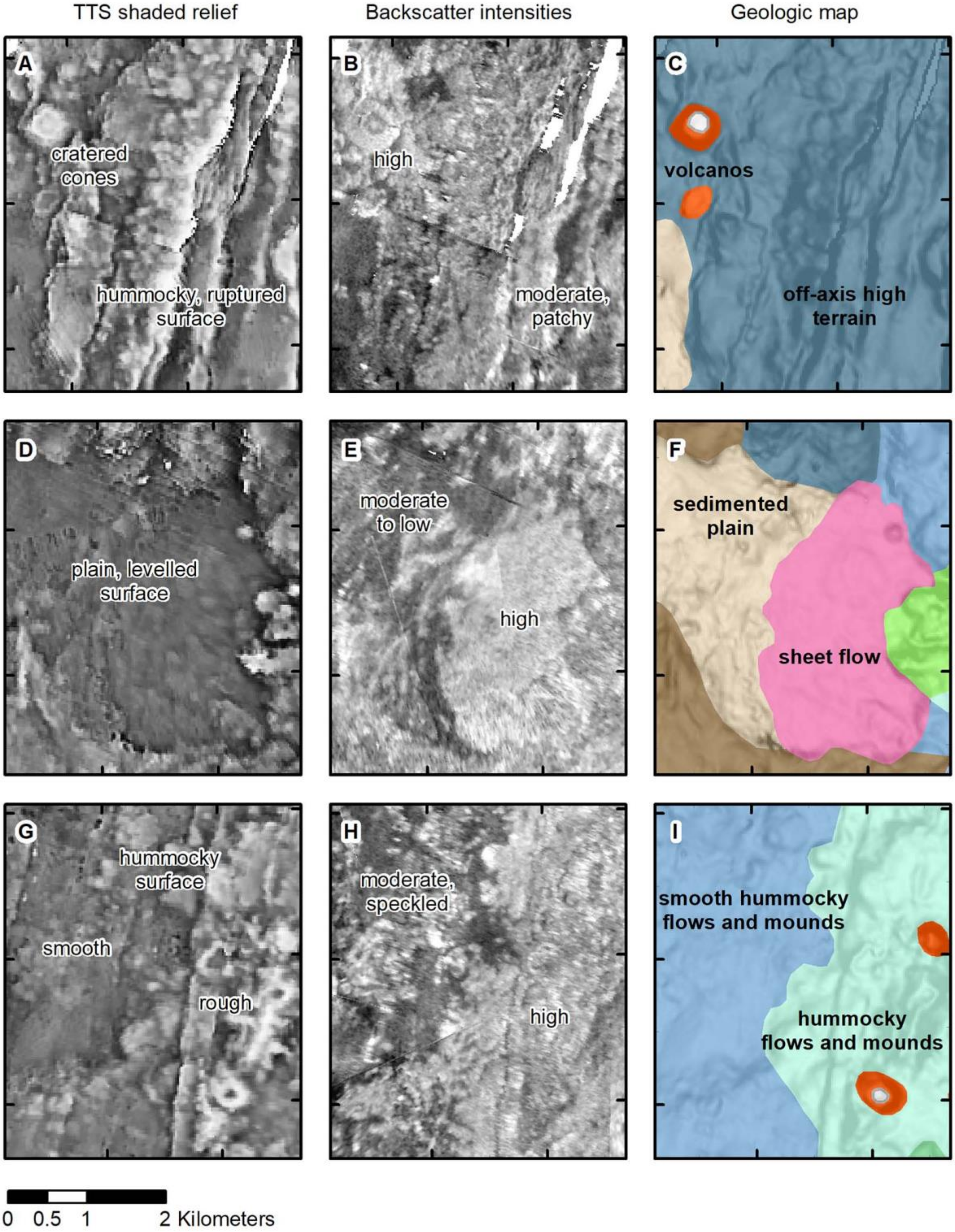
TTS shaded relief
Backscatter intensities
Geologic map
A
cratered cones
hummocky, ruptured surface
B
high
moderate, patchy
C
volcanos
off-axis high terrain
D
plain, levelled surface
E
moderate to low
high
F
sedimented plain
sheet flow
G
hummocky surface
smooth
rough
H
moderate, speckled
high
I
smooth hummocky flows and mounds
hummocky flows and mounds
0 0.5 1 2 Kilometers

930

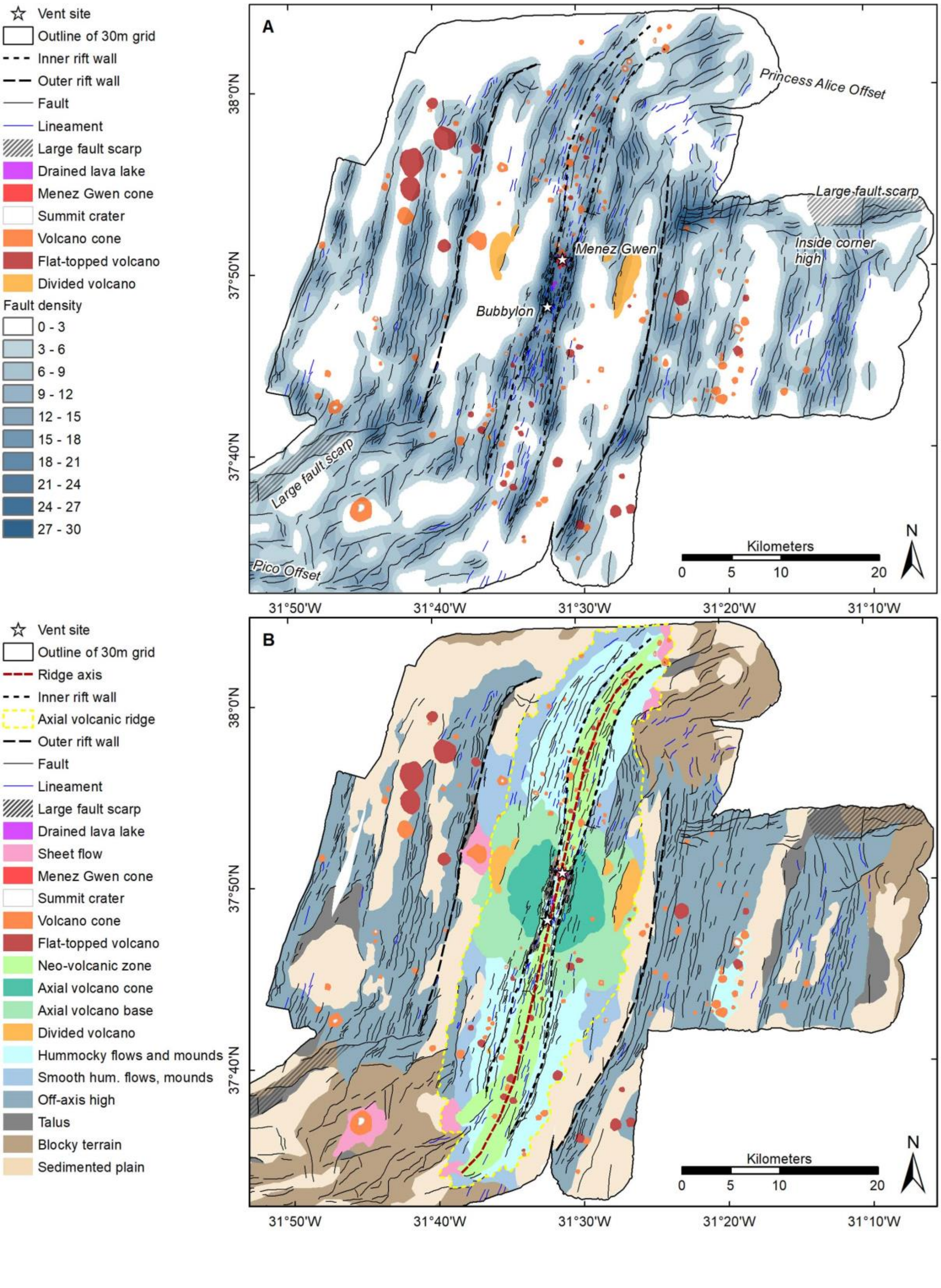
Vent site
Outline of 30m grid
Inner rift wall
Outer rift wall
Fault
Lineament
Large fault scarp
Drained lava lake
Menez Gwen cone
Summit crater
Volcano cone
Flat-topped volcano
Divided volcano
Fault density
0 - 3
3 - 6
6 - 9
9 - 12
12 - 15
15 - 18
18 - 21
21 - 24
24 - 27
27 - 30
A
Princess Alice Offset
Large fault scarp
Inside corner high
Menez Gwen
Bubbylon
Large fault scarp
Pico Offset
Kilometers
0 5 10 20
N
38°0'N
37°50'N
37°40'N
31°50'W 31°40'W 31°30'W 31°20'W 31°10'W
Vent site
Outline of 30m grid
Ridge axis
Inner rift wall
Axial volcanic ridge
Outer rift wall
Fault
Lineament
Large fault scarp
Drained lava lake
Sheet flow
Menez Gwen cone
Summit crater
Volcano cone
Flat-topped volcano
Neo-volcanic zone
Axial volcano cone
Axial volcano base
Divided volcano
Hummocky flows and mounds
Smooth hum. flows, mounds
Off-axis high
Talus
Blocky terrain
Sedimented plain
B
Kilometers
0 5 10 20
N
38°0'N
37°50'N
37°40'N
31°50'W 31°40'W 31°30'W 31°20'W 31°10'W

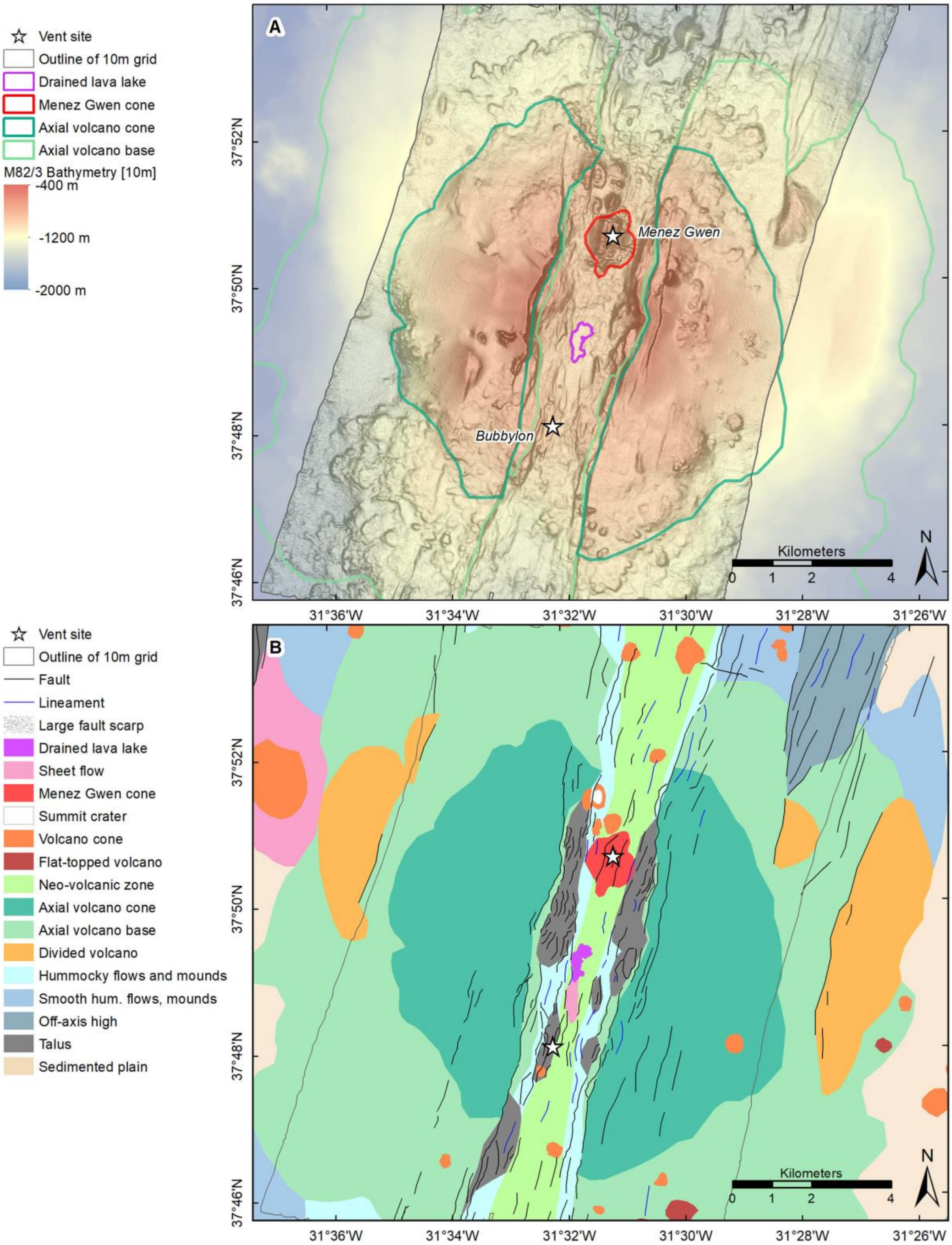
Vent site
Outline of 10m grid
Drained lava lake
Menez Gwen cone
Axial volcano cone
Axial volcano base
M82/3 Bathymetry [10m]
-400 m
-1200 m
-2000 m
A
Menez Gwen
Bubbylon
Kilometers
0 1 2 4
N
37°52'N
37°50'N
37°48'N
37°46'N
31°36'W
31°34'W
31°32'W
31°30'W
31°28'W
31°26'W
Vent site
Outline of 10m grid
Fault
Lineament
Large fault scarp
Drained lava lake
Sheet flow
Menez Gwen cone
Summit crater
Volcano cone
Flat-topped volcano
Neo-volcanic zone
Axial volcano cone
Axial volcano base
Divided volcano
Hummocky flows and mounds
Smooth hum. flows, mounds
Off-axis high
Talus
Sedimented plain
B
Kilometers
0 1 2 4
N

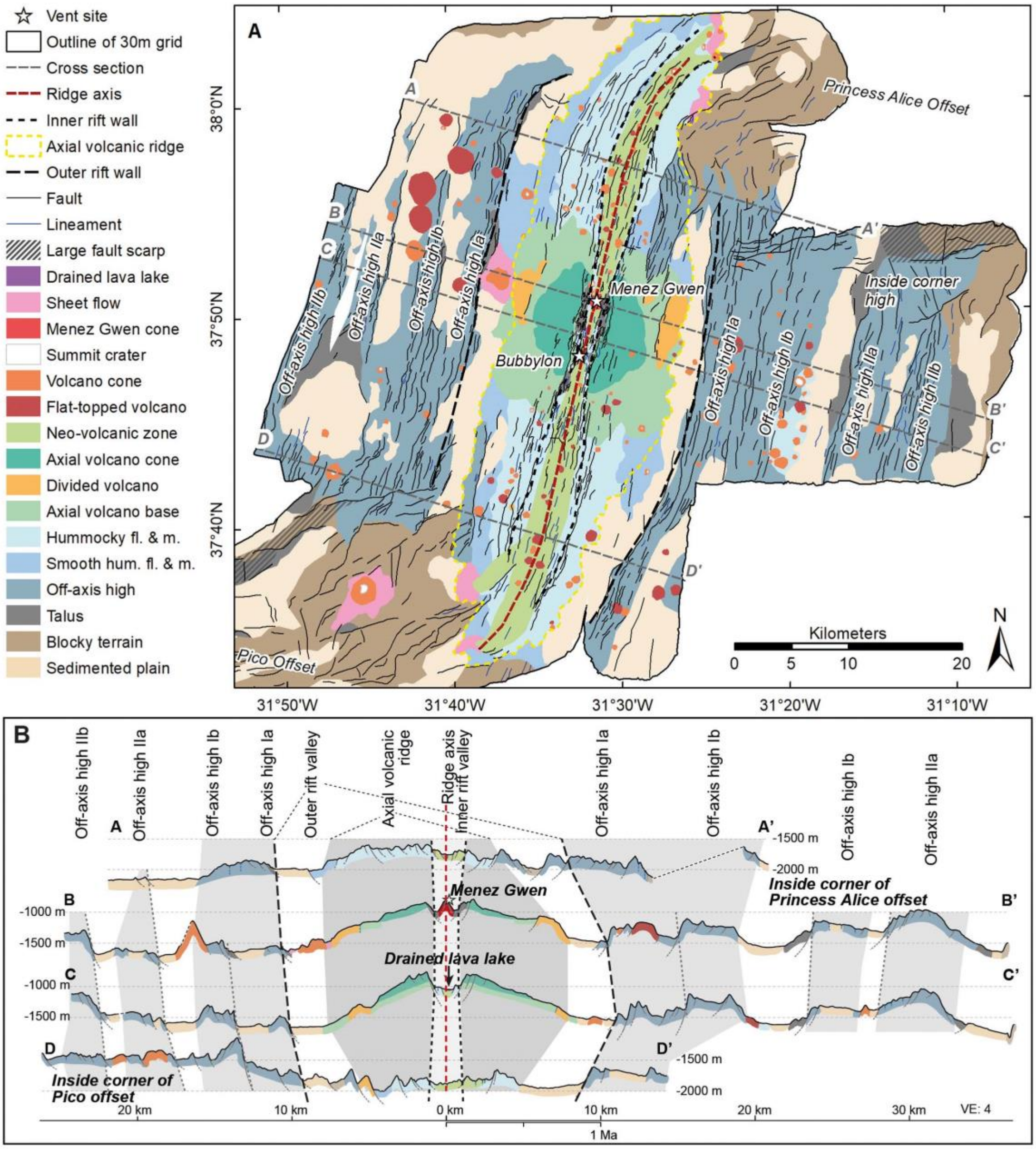
A
B
Vent site
Outline of 30m grid
Cross section
Ridge axis
Inner rift wall
Axial volcanic ridge
Outer rift wall
Fault
Lineament
Large fault scarp
Drained lava lake
Sheet flow
Menez Gwen cone
Summit crater
Volcano cone
Flat-topped volcano
Neo-volcanic zone
Axial volcano cone
Divided volcano
Axial volcano base
Hummocky fl. & m.
Smooth hum. fl. & m.
Off-axis high
Talus
Blocky terrain
Sedimented plain
Princess Alice Offset
Pico Offset
Menez Gwen
Bubbylon
Inside corner high
Kilometers
Drained lava lake
Inside corner of Princess Alice offset
Inside corner of Pico offset
VE: 4
1 Ma

933

Table 1. Overview of geological mapping criteria for supervised classification of DEMs derived from ship-based MBES data.

Morphology pattern	**Slope**	**Rugosity**	**Backscatter**	**Relations**	**Outline**	**Minimum Size**	**Mapped feature**	**Comment**
Elementary features								
Scarp; linear step in topography	Distinct, elongated area of high slope angle	Very high over the entire scarp	Depends on direction of illumination	Usually face the ridge axis in this setting; slightly curved on talus fans	Base of the scarp, concave relief change	10 times spatial resolution	*Fault*	For various fault stages see Allerton et al. (1995)
Linear feature without clear relief	Linear change in topography without any detectable dip	Distinct, elongated change	Depends on direction of illumination	-	Along centre	10 times spatial resolution	*Lineament*	
Cone; protruding round to dome-like elevations with steep flanks	High to very high; distinct convex-shape at bottom of flank	Prominent, circles of high rugosity, with a low in its centre	High, sharp outline	Often to hummocky terrain; partly to lava flows	Convex-shaped slope change	Ca. 30 m height, might differ on slopes	*Volcano cone*	May has summit depression or crater
Flat-topped cone; protruding round to dome-like elevations with steep flanks	Steep flanks; wide, flat summit	Prominent, concentric changes	High on flanks, may be lower on summit	Often to hummocky terrain	Convex-shaped slope change	Diameter of 10 times spatial resolution	*Flat-topped volcano*	Characteristic height to width ratio of ca. 1:10
Funnel-shaped depression on volcanic forms	Distinct, medium to high slopes	Prominent, concentric change	Usually high	On or within volcanic summits	Concave-shaped slope change at crater rim	3 times spatial resolution	*Crater*	
Terrain types								
Wide flats of even seafloor	None, homogeneous; may has minor inclination on a large scale	Homogeneously low	Homogeneously low	Area with only few elementary features within	Usually bound by slope changes	30 x 100 DEM cells	*Sedimented plain*	Outline partly difficult to determine due to gradational contacts
Limited areas of flat, even seafloor	None, homogeneous; may has minor, overall inclination	Homogeneously low	High to very high, homogeneous	To volcanic forms	Slope changes, backscatter signal	20 x 100 DEM cells	*Sheet flow*	
Elevated terrain with unconfined depressions and mounds	Highly variable; dominated by rounded or circular changes	Variable; 'cauliflower' pattern	High to very high	Usually ruptured by faults	Traces margins of high backscatter intensities; occasional slope changes	30 x 100 DEM cells	*Hummocky flows and mounds*	Outline partly difficult to determine due to gradational contacts
Elevated terrain with unconfined depressions and mounds	Highly variable; dominated by rounded or circular changes	Variable; 'cauliflower' pattern	Highest intensities	Usually contains short faults and lineaments, and	Traces margins of highest backscatter intensities, inward facing faults	20 x 100 DEM cells	*Neo-volcanic zone*	Outline partly difficult to determine due to gradational contacts

Morphology pattern	Slope	Rugosity	Backscatter	Relations	Outline	Minimum Size	Mapped feature	Comment
				plenty of small volcanic cones				
Elevated terrain with smooth, unconfined depressions and mounds	Variable; dominated by rounded or circular changes	Variable; smooth ‘cauliflower’ pattern	Moderate to high	Usually ruptured by faults	Traces margins of moderate backscatter intensities; occasional slope changes	30 x 100 DEM cells	*Sedimented hummocky flows and mounds*	Outline partly difficult to determine due to gradational contacts
Elevated terrain with smoother, unconfined depressions and mounds	Variable; rounded and elongated, straight slopes	Variable; interrupted, smooth ‘cauliflower’ pattern	Patches of low to high intensities	Intensely ruptured by large faults	Slope changes	30 x 100 DEM cells	*Off-axis high*	Outline partly difficult to determine due to gradational contacts
Rough, structure-less terrain with elongated depressions and highs	Highly variable on small to large scale; partly elongated, no preferred direction	High variability on various scales; straight features dominate	No defined pattern; rough topography distorts signal	Usually within large scale depressions; intensely ruptured by large faults	Changes in slope and rugosity	30 x 100 DEM cells	*Blocky terrain*	Outline partly difficult to determine due to gradational contacts
Structure-less terrain in small, fan-shaped patches	Smoother slope on underlying steep slope	Moderate to high	No pattern; underlying topography distorts signal	Usually aligned to large faults	Changes in slope and rugosity	30 x 30 DEM cells	*Talus*	Outline partly difficult to determine due to gradational contacts